Batteries & Supercaps

Research Article
doi.org/10.1002/batt.202200495

Chemistry Europe
European Chemical Societies Publishing

www.batteries-supercaps.org

Synthesis, Electrochemistry, and Thermal Stability of High-Energy Ball-Milled Silicon-based Alloy Anodes in Lithium-Ion Batteries**

Xingyu Zhang[+],[a] Luqi Wang[+],[c] Tianye Zheng,[a] and Kwok-ho Lam*[a, b]

The fast capacity degradation of silicon-based anodes significantly limits the application in lithium-ion battery (LIB) industries. Recently, Si–CuO composites have been reported as promising anodes in terms of being cost-effective and technically feasible, but improved cycle stability is still desired. This work introduces a proper amount of NiO into the Si–CuO composites via a facile high-energy ball-milling method. The study reveals that compared to the binary Si-CuO composites, Si–CuO–NiO samples have less pronounced volume change during the cycles due to the formation of rich-Si $NiSi_2$. More specifically, $Si_{87.5}(CuO)_{3.4}(NiO)_{9.1}$ shows the highest 100-cycle capacity retention of ~86.9% at 0.2 C with an average coulombic efficiency of ~99.4%. Moreover, the thermal stability investigation demonstrates that the temperature of 600 °C is suitable to coat a carbon layer on $Si_{87.5}(CuO)_{3.4}(NiO)_{9.1}$, where the microstructure and the uniform element distribution produced in the milling process as well as the suppression to the cr-$Li_{3.75}Si$ formation can be maintained to the maximum extent, thus with further enhanced electrochemical performance.

Introduction

Conventional graphite anode in lithium-ion batteries (LIBs) has not yet met the market demand due to its limited capacity, ~370 mAh g^{-1} or ~719 Ah L^{-1}.[1,2] Compared with graphite, silicon (Si) has a higher specific capacity of ~3580 mAh g^{-1} (or ~2194 Ah L^{-1}) at room temperature.[2] Correspondingly, it could realize a ~34% increase of volumetric energy density in a full cell when coupling with $LiCoO_2$ cathode based on the model proposed by M.N. Obrovac et al.[3] These merits make Si one of the most promising anodes for the next generation of LIBs. Nevertheless, one of the biggest challenges faced by Si anodes is the fast capacity fading due to the huge volume changes during the lithiation-delithiation processes.[2] To be specific, Li insertion could increase the volume of Si by ~280%, while Li extraction would cause a lattice shrinkage.[2] Such repetitive volume expansion and contraction during cycling would lead to the disruption of Si particles and unstable solid electrolyte interphase (SEI), resulting in poor electrical contact between active materials, mechanical failure of the electrode, and a higher impedance in the cell.[4–6] Accordingly, some Li^+ would likely be trapped in the bulk of Si during the delithiation process, and be irreversibly consumed due to the secondary SEI formation.[7] Therefore, the strategy to alleviate the large volume change of Si anode is critical for achieving the ideal electrochemical performance.

Applying transition metal elements (M) to alloy with Si and form Si/metal silicides can effectively mitigate the aforementioned issues. The metal silicides are generally inactive to Li^+[8] or have limited lithiation capacities.[9,10] The volume change can be diluted when Si particles are dispersed in the inactive matrix.[11,12] Although with the sacrifice of some gravimetric specific capacity, the resulting volumetric specific capacity and energy density in Si–M alloy anodes are still quite competitive.[12] Practically, high-energy ball-milling (HEBM) is an efficient method for synthesizing Si–M alloys. During the milling process, the nanocrystalline Si with a high amorphous degree can be obtained, which is also considered a positive effect on the cycle performance.[13,14] Based on these reasons, there are already extensive works focusing on fabricating Si–M alloy anodes via the HEBM method in recent years, e.g., Si–Mo,[15] Si–W,[16] Si–Mn,[17] Si–Ti,[18] Si–Ni,[19] Si–Fe,[8] and Si–Cu[20] systems. The investigations indicate the enormous application potential of ball-milled Si–M alloy anodes, but better electrochemical performance is still desirable for commercialization.[21]

Recent studies reveal that introducing the O element into Si–M alloy anodes could improve the cycle performance and

[a] X. Zhang,[+] Dr. T. Zheng, Dr. K.-h. Lam
Department of Electrical Engineering
The Hong Kong Polytechnic University
Hung Hom, Kowloon (Hong Kong)
E-mail: kokokh.lam@polyu.edu.hk
[b] Dr. K.-h. Lam
James Watt School of Engineering
University of Glasgow
Glasgow, Scotland (United Kingdom)
E-mail: kwokho.lam@glasgow.ac.uk
[c] L. Wang[+]
Faculty of Science and Engineering
The University of Manchester
Manchester, England (United Kingdom)
[+] These authors contributed equally to this work.

[**] A previous version of this manuscript has been deposited on a preprint server (https://doi.org/10.26434/chemrxiv-2022-rqmcz-v2).

Supporting information for this article is available on the WWW under https://doi.org/10.1002/batt.202200495

Research Article
doi.org/10.1002/batt.202200495
Chemistry Europe
European Chemical Societies Publishing

coulombic efficiency.[21,22] Besides maintaining the merit of silicides, amorphous Si oxides can be intercalated by Li^+ to produce inactive Li silicates in the first cycle,[21] which are significantly helpful to buffer the large volume change of Si and yield a more stable SEI and longer life cycle.[23] Nevertheless, Si oxides are usually formed under the high-temperature condition (~1400 °C) via the reaction between Si and SiO_2, which is an energy-consuming and expensive process.[24–26] A low-cost and facile method for introducing the O element would be highly desired for academia and commercialization. As the HEBM method effectively produces Si–M alloy anodes on a large scale, one of the feasible solutions is to use a metal oxide to alloy with Si. Under the non-equilibrium condition driven by high mechanical energy,[27] it is expected to produce metal silicides and amorphous Si oxides simultaneously. The relevant studies have been reported,[27–29] where CuO is chosen as a doped metal oxide source. With the synergistic effect of the in-situ generated Cu_3Si and Si oxides, the ball-milled Si–CuO composites yield enhanced cycle stabilities. More importantly, the fabrication of Si–CuO composites is claimed to be financial feasibility and environmentally compatible, showing excellent application promise.[9] Thus, further improvement of the all-around performance of this system will be meaningful and valuable.

Herein, we propose a novel way of introducing NiO to the ball-milled Si–CuO composites to optimize the electrochemical performance. The reasons for choosing NiO are as follows: 1) the introduction of NiO could also provide the O element for forming Si oxides. Simultaneously, the Ni element is predicted to react with Si to form $NiSi_2$;[19] 2) different from Cu_3Si, $NiSi_2$ is a Si-rich compound, so more active Si is expected to be stored in the metal silicide when part of CuO is replaced with NiO. Correspondingly, the volume change of Si-based anodes would be effectively relieved;[12] and 3) the ball-milled Si-based precursors often need a post-treatment of coating a protective carbon layer for further enhancing the electrical conductivity, stabilizing the SEI, and prolonging the life cycle.[16,27,28] However, to carbonize the coated organic species as much as possible, this post-treatment is generally a high-temperature process,[21] which is usually required to maintain the nano-crystalline/amorphous microstructure of ball-milled Si-based precursors after the calcination.[5,15] Due to the higher melting point of $NiSi_2$ (~993 °C) than that of Cu_3Si (~802 °C), the introduction of NiO would be expected to impart higher temperature tolerance onto the composites.[15,16] Therefore, we propose the HEBM-synthesized Si–CuO–NiO composites in this study and systematically investigate the materials' micromorphology and composition, electrochemical behavior, cycle performance, and thermal stability.

Results and Discussion

Material characterization

The morphology of all the samples is shown in Figure 1 with the medium particle size (D_{50}) stated. The shape of the pristine Si particles is irregular under SEM with a relatively larger D_{50} of ~3.9 μm. As for all the other ball-milled samples, no noticeable difference in morphology and particle size is observed under the chosen magnification with the D_{50} of 1.6–2.4 μm. The similar particle size here may help to ensure fair comparisons, i.e., the effect of particle sizes is minimized. Consequently, the influence of NiO additions on the electrochemical performances of the Si-based electrodes can be investigated and discussed in isolation.

Figure 2 shows the diffraction patterns of pure Si and the ball-milled samples, and the confirmation of phases is based on ICDD PDF-4+ released in 2009. There are no diffraction peaks related to CuO/NiO in Figure 2, indicating that both oxides have already reacted with Si and/or partly exist in the amorphous state. The diffractograms of pure Si and Si–CuO samples are shown in Figure 2(a). The former exhibits sharp peaks at 28.4°, 47.3°, 56.1°, 69.1° and 76.3° which are in line with crystalline Si (PDF#04-002-0891). Differently, Si in the Si–CuO samples exhibits a significantly lower grain size and

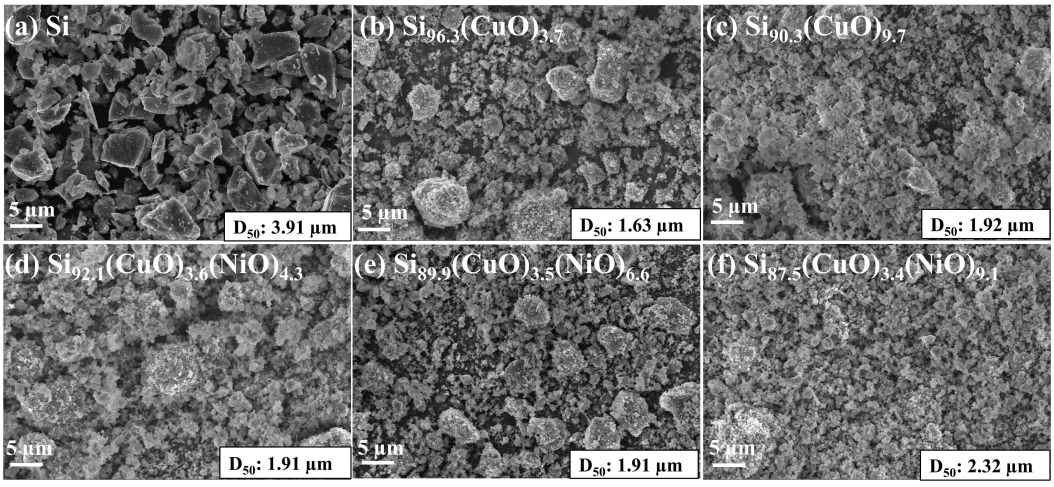

Figure 1. SEM pictures of Si, ball-milled Si–CuO, and Si–CuO–NiO samples.

Research Article
doi.org/10.1002/batt.202200495
Chemistry Europe
European Chemical Societies Publishing

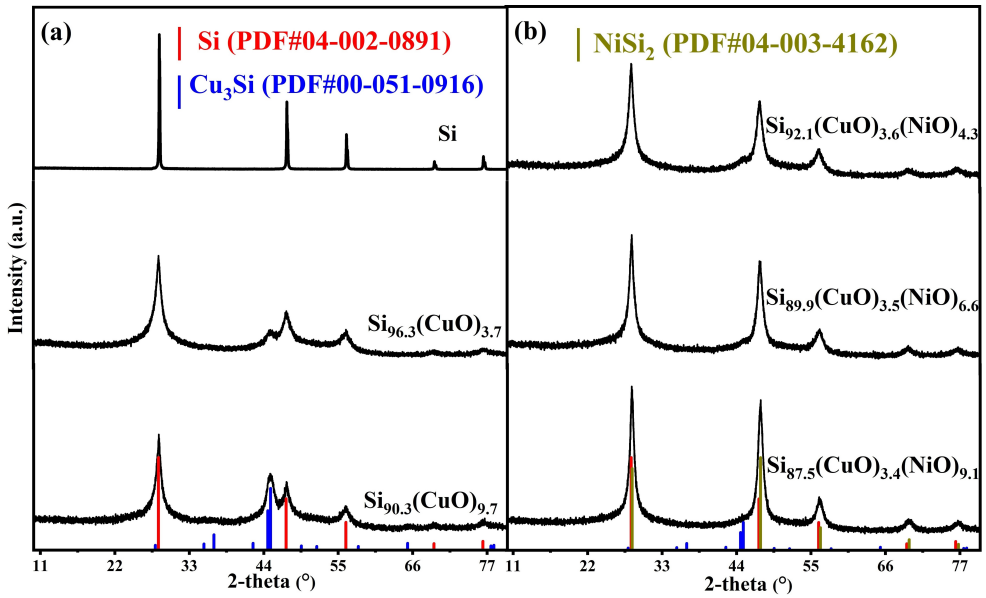

Figure 2. XRD patterns of a) Si and Si–CuO samples and b) Si–CuO–NiO samples.

crystallinity, as supported by the peak broadening. Together with the Scherrer equation, the average grain size of Si in each sample can be estimated, decreasing from ~80 nm in pure Si to ~8 nm in the Si–CuO samples. The two overlapped peaks at 44.5° and 44.9° in $Si_{96.3}(CuO)_{3.7}$ and $Si_{90.3}(CuO)_{9.7}$ indicate the formation of Cu_3Si (PDF#00-051-0916) with the grain size of ~7 nm and their relative intensities increases with the introduction of higher CuO contents.

The peaks related to Cu_3Si become inconspicuous in the diffractograms of the three Si–CuO–NiO samples in Figure 2(b), implying a higher amorphization degree of Cu_3Si.[27,28] $NiSi_2$ is expected to be formed in this system with the diffraction peaks overlapping the ones of Si, and thus difficult to distinguish.[30] However, the relative peak intensities between these two phases are different, which can assist us in identifying the existence of $NiSi_2$.[31] Figure S1 shows the phase evolution of $Si_{87.5}(CuO)_{3.4}(NiO)_{9.1}$ during the milling process. With the extension of the milling time, the peaks related to NiO gradually become weaker, eventually disappearing after 4-hour milling. At the same time, the relative intensity of the peak at 47.3° is slowly increasing, which corresponds to the strongest peak of $NiSi_2$ (PDF#04-003-4126, referring to ICDD PDF-4+). Eventually, the ratio (100:91.7) of the peaks at 28.4° and 47.3° in $Si_{87.5}(CuO)_{3.4}(NiO)_{9.1}$ through 4-hour milling is better consistent with the one (88.1:100) of $NiSi_2$ in the standard card, whereas this value in pristine Si and Si–CuO samples are much closer to the theoretical value of Si (100:55.5). In addition, no peaks related to other Ni silicides are observed, further suggesting the possibility of crystalline $NiSi_2$ formation in the Si–CuO–NiO samples.

The XPS technique is employed to investigate the chemical state of different elements in the samples of $Si_{96.3}(CuO)_{3.7}$, $Si_{90.3}(CuO)_{9.7}$, $Si_{89.9}(CuO)_{3.5}(NiO)_{6.6}$, and $Si_{87.5}(CuO)_{3.4}(NiO)_{9.1}$. Figure 3(a) shows the full spectra, and the peaks related to Si 2p, O 1s, Cu 2p, and Ni 2p can be observed, confirming the existence of Si, O, Cu, and Ni elements on the surface of the samples. Figure 3(b) presents the original XPS spectra and the fitting curves for Si 2p, revealing that the chemical state of the Si element on the sample surfaces is similar. The peaks at around 98.8 eV and 99.4 eV are assigned to Si $2p_{3/2}$ and Si $2p_{1/2}$, most likely from pure Si and Cu_3Si[32,33]. Meanwhile, the peaks at around 103 eV and 101.2 eV are suggested to be contributed by SiO_2 and SiO_x ($0<x<2$),[29,32] respectively. It can be seen that SiO_2 is the major Si oxide on the surfaces of ball-milled samples. Then we calculate the fitting peak area ratios of different Si oxidation states in Si 2p spectra, as shown in Table S2. With the increase of metal oxides, the fraction of the fitted peak areas assigned to SiO_2 constantly rises, from 36.4% in $Si_{96.3}(CuO)_{3.7}$ to 65.5% in $Si_{87.5}(CuO)_{3.4}(NiO)_{9.1}$. This positive correlation implies that a part of SiO_2 may be contributed by the Si and metal oxides reaction.

Figure 3(c) presents the Cu 2p spectra of the chosen samples. The peaks at around 932.6 eV and 952.6 eV show that the chemical state of Cu element on the surface is mainly in its zero valence instead of +2 valence, further proving the reduction reaction between CuO and Si during the ball-milling process. Due to the identical XPS binding energy of Cu $2p_{3/2}$ in Cu_3Si and pure Cu,[33] in conjunction with the XRD results, it is suggested that the two peaks most likely originate from the elemental Cu of produced Cu_3Si. The Ni 2p spectra of $Si_{89.9}(CuO)_{3.5}(NiO)_{6.6}$ and $Si_{87.5}(CuO)_{3.4}(NiO)_{9.1}$ can be seen in Figure 3(d). The peaks at around 853.1 eV and 870.5 eV are assigned to Ni $2p_{3/2}$ and Ni $2p_{1/2}$ of Ni silicide, respectively, which are closer to the ones of $Ni_{31}Si_{12}$ or Ni_2Si instead of $NiSi_2$.[34] This phenomenon may be due to the partial oxidation of Si in pre-formed $NiSi_2$ on the surfaces, causing the transformation of Si–Ni alloys from a rich-Si state to a rich-Ni state.[35] Nevertheless, such an oxidation process is assumed to be limited by the kinetics[35] with a minor presence of $Ni_{31}Si_{12}$ or Ni_2Si, thereby playing an insignificant role in the electro-

Research Article
doi.org/10.1002/batt.202200495
Chemistry Europe
European Chemical Societies Publishing

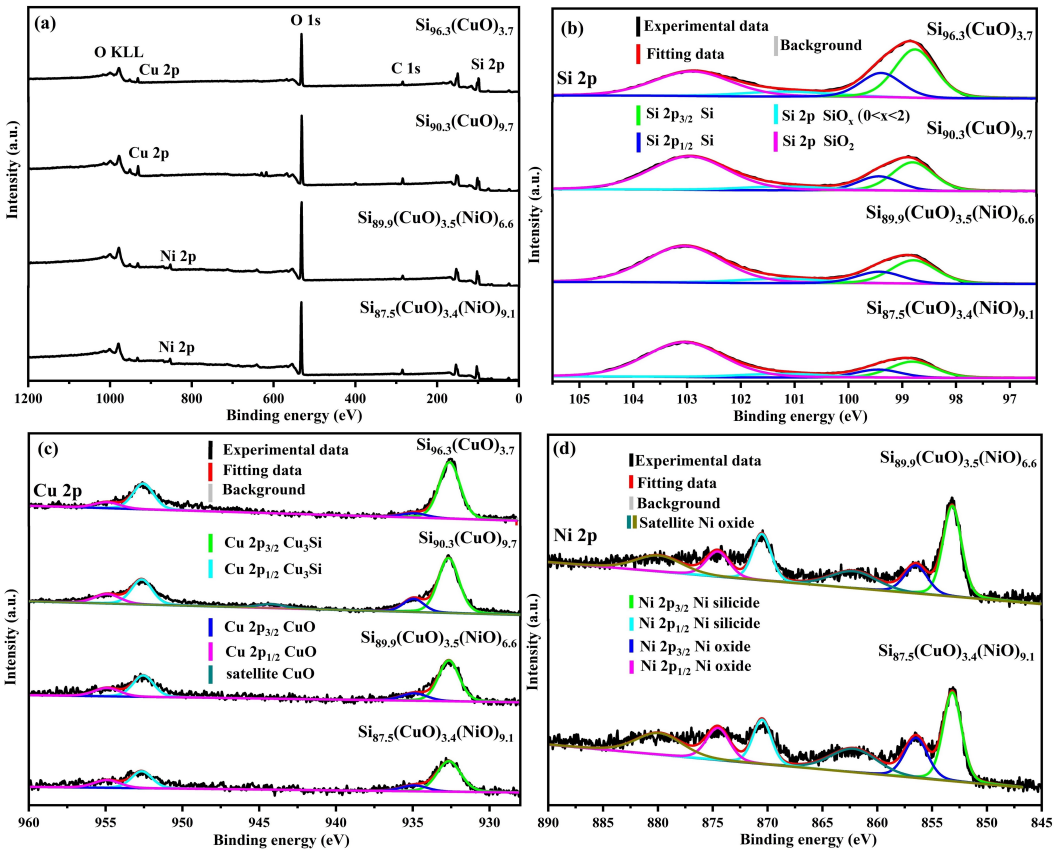

Figure 3. a) XPS full spectra, b) Si 2p spectra, c) Cu 2p spectra of $Si_{96.3}(CuO)_{3.7}$, $Si_{90.3}(CuO)_{9.7}$, $Si_{89.9}(CuO)_{3.5}(NiO)_{6.6}$ and $Si_{87.5}(CuO)_{3.4}(NiO)_{9.1}$ samples. d) Ni 2p spectra of $Si_{89.9}(CuO)_{3.5}(NiO)_{6.6}$ and $Si_{87.5}(CuO)_{3.4}(NiO)_{9.1}$.

chemical performance. In addition, the peaks assigned to CuO[29] and Ni oxides[36] in the Cu 2p and Ni 2p spectra can also be found in Figures 3(c) and (d), indicating that there might be the minor amorphous metal oxides remaining in the Si–CuO and the Si–CuO–NiO samples after the milling process. To sum up, the XPS results demonstrate the existence of Si, O, Cu, and Ni elements in the ball-milled samples and the successful reduction of metal oxides by Si.

To confirm the microstructure and the element distribution, the typical samples of $Si_{90.3}(CuO)_{9.7}$ and $Si_{89.9}(CuO)_{3.5}(NiO)_{6.6}$ are chosen to undergo TEM and STEM tests considering their same mass proportion of the metal oxides. According to the bright field (BF) images shown in Figures 4(a, i) and HRTEM images of Figures 4(b, j), the ball-milled Si-based particles are mainly composed of many dispersed nano-crystallites with some amorphous regions. These amorphous regions are possibly amorphous Si oxides or residual metal oxides based on the XRD and XPS analysis. According to the SAED pattern in Figures 4(c, k), we could know the nano-crystallites derived from Si, Cu_3Si, and $NiSi_2$, respectively. As mentioned above, Si and $NiSi_2$ have similar crystalline structures with almost identical lattice parameters.[30] Thus, they are represented by the same diffraction rings. Combining the XRD result, crystalline $NiSi_2$ is the primary Si–Ni alloy in $Si_{89.9}(CuO)_{3.5}(NiO)_{6.6}$.

Besides, the homogenous element distribution in ball-milled Si-based anodes is another crucial factor for better cycling performance.[6,37] The bright regions in STEM images (Figures 4(d and l) denote the doped metal elements. The element mapping and the related substitution overlaps (Figures 4e–h, m–q) further confirm the existence of Si, O, Cu, and Ni elements, consistent with the XPS results. All the elements in $Si_{89.9}(CuO)_{3.5}(NiO)_{6.6}$ are homogeneously distributed. However, the Cu element in $Si_{90.3}(CuO)_{9.7}$ exhibits agglomerations to some extent within the scanned region.

Herein, combining the results of XRD, XPS, TEM, and STEM, we conclude that after the 4-hour ball-milling process for the Si–CuO and Si–CuO–NiO samples, the obtained samples mainly consist of nanocrystalline Si, doped metal silicide, and amorphous Si oxides. At the same time, a more uniform element distribution is observed for $Si_{89.9}(CuO)_{3.5}(NiO)_{6.6}$.

Electrochemical characterization

The electrochemical behaviors of Si, Si–CuO, and Si–CuO–NiO samples are investigated by presenting their differential capacity-voltage (d*Q*/d*V*) curves in Figures 5(a–f) and corresponding voltage-capacity curves in Figures 5(g–l). The 1st lithiation for all samples shows distinctive features from the subsequent cycles, giving a pronounced lithiation peak at around 0.1 V versus Li/Li^+ in the d*Q*/d*V* curves corresponding to a lithiation plateau at the same potential in the voltage-

Research Article
doi.org/10.1002/batt.202200495
Chemistry Europe
European Chemical Societies Publishing

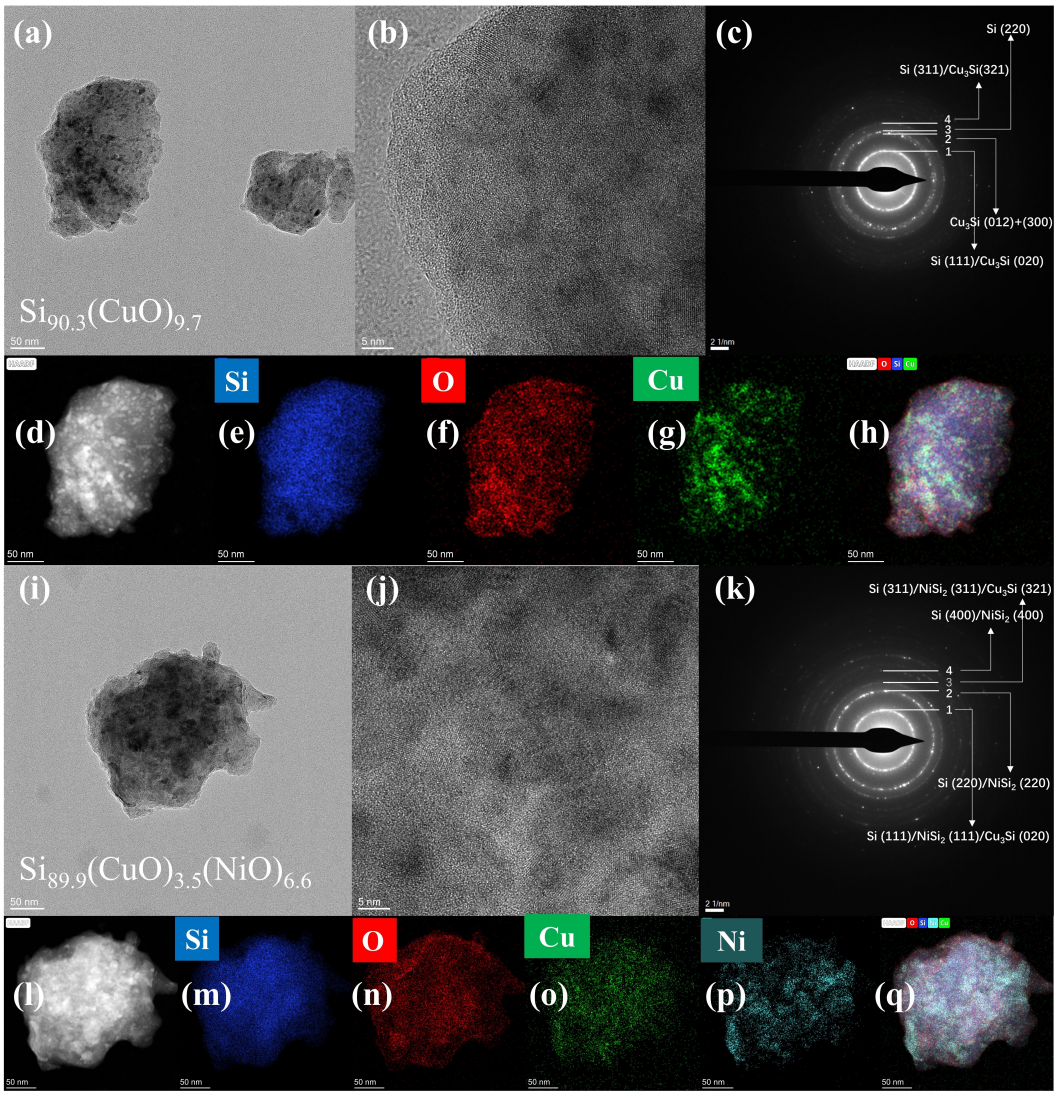

Figure 4. a and i) BF images, b and j) HRTEM images, c and k) SAED patterns, d and l) STEM images, e–g and m–p) element maps, and h and q) element substitution overlaps of $Si_{90.3}(CuO)_{9.7}$ and $Si_{89.9}(CuO)_{3.5}(NiO)_{6.6}$.

capacity curves. This lithiation peak is indicative of a two-phase coexistence region of cr-Si and amorphous Li_xSi ($0 < x \leq 3.5$).[38,39] Compared with pure Si, this peak becomes broader for the Si–CuO and Si–CuO–NiO samples, which may be due to the microstructure change of the ball-milled Si particles with lower crystallinity.[18,19]

For the 1st delithaition, only one prominent peak at ~0.43 V in the d*Q*/d*V* curve of pristine Si can be seen (Figure 5a). In contrast, two pronounced peaks at around 0.3 V and 0.5 V vs. Li/Li^+ exist in the d*Q*/d*V* curves of the Si–CuO and Si–CuO–NiO samples, representing the transformation from a-$Li_{3.5}Si$ to a-Li_2Si and from a-Li_2Si to a-Si, respectively.[38,39] The appearance of a 0.43 V delithiation peak is a sign of cr-$Li_{3.75}Si$ generated in the Si bulk, which is considered detrimental to the electrochemical performance due to the mismatched volume change in the phase boundary between cr-$Li_{3.75}Si$ and amorphous Li_xSi alloy.[40] Correspondingly, pristine Si has the lowest initial coulombic efficiency (ICE) of 76.4% (Figure 5g) in this study, suggested to be partly caused by the generation of cr-$Li_{3.75}Si$ causing a more extensive fracture of the Si bulk during the first delithiation.[40] On the other hand, this peak becomes obscure in the dQ/dV curves of the Si–CuO and Si–CuO–NiO samples, mainly ascribed to stress-voltage coupling induced by formed Cu_3Si and $NiSi_2$.[41,42] These metal silicides can impose compressive stress on the expanded Si bulk during the lithiation; for example, the higher compressive stress of 1.5 GPa will negatively shift the lithiation potential as much as 200 mV to completely avoid the formation of cr-$Li_{3.75}Si$.[2,41,42] A negative correlation is observed between the ICEs and the metal oxide content for the ball-milled samples. The addition of metal oxides with different amounts leads to an ICE variation from 85.2% in $Si_{96.3}(CuO)_{3.7}$ to 80.1% in $Si_{87.5}(CuO)_{3.4}(NiO)_{9.1}$ (Figures 5h–l). This correlation could partly be caused by the irreversible lithiation of the formed Si oxides[21] and/or native metal oxides of the as-prepared samples.[43,44]

Research Article
doi.org/10.1002/batt.202200495
Chemistry Europe
European Chemical Societies Publishing

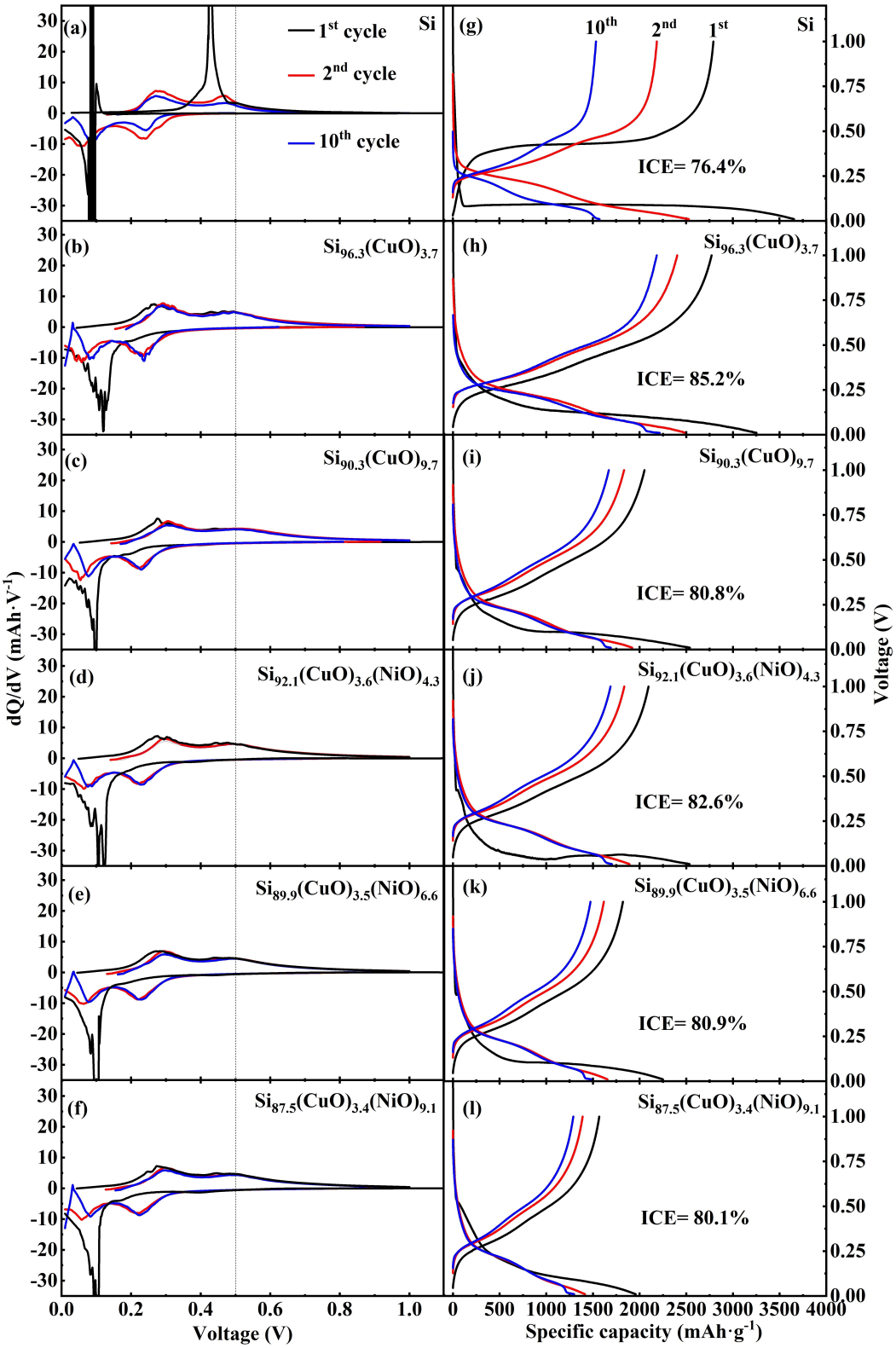

Figure 5. a–f) d*Q*/d*V*-voltage curves of the 1st, 2nd and 10th cycle of Si, Si–CuO and Si–CuO–NiO samples, and g–l) their corresponding voltage-capacity curves.

Since the second cycle, two broad lithiation peaks at around 0.06 V and 0.23 V vs. Li/Li$^+$ appear in the d*Q*/d*V* curves for all the samples, corresponding to two sloping plateaus in the voltage-capacity curves. These two peaks indicate the formation of amorphous Li_2Si and $Li_{3.5}Si$.[45] In contrast, the delithiation peak for cr-$Li_{3.75}Si$ is always absent among the ball-milled samples in the later cycles, similar to the 1st delithiation. In brief, both the ball-milled Si–CuO and Si–CuO–NiO samples

Research Article
doi.org/10.1002/batt.202200495
Chemistry Europe
European Chemical Societies Publishing

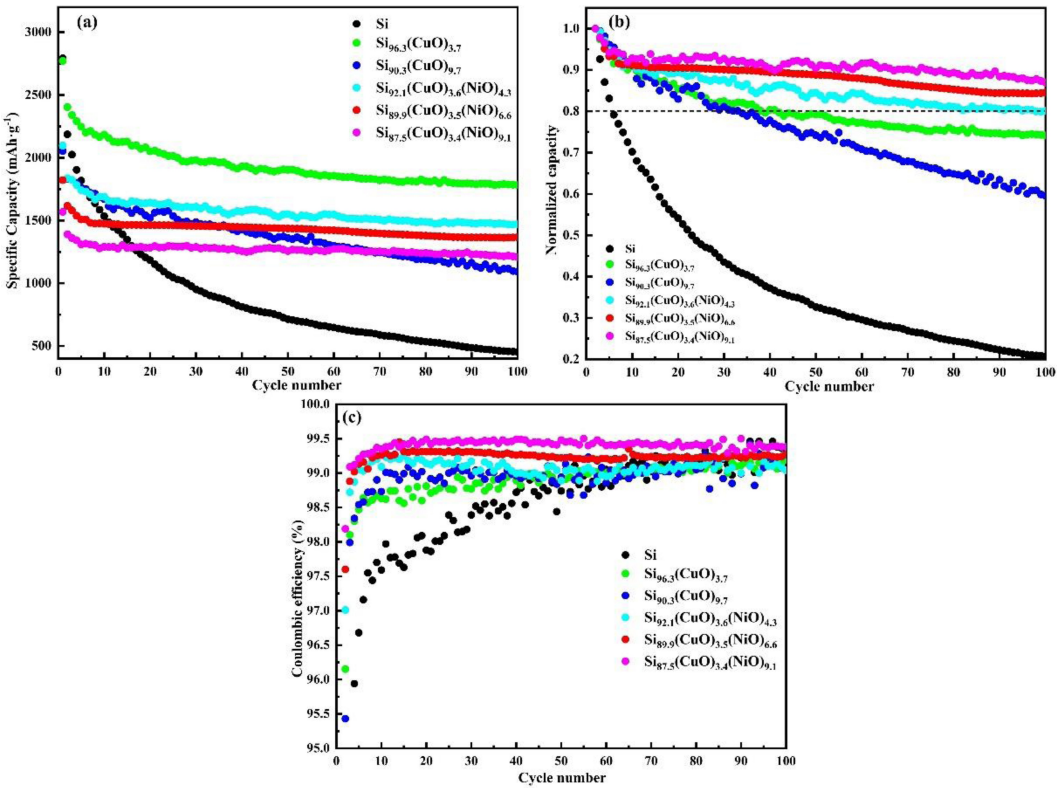

Figure 6. a) Specific delithiation capacity vs. cycle number, b) normalized delithiation capacity (concerning the second cycle) vs. cycle number, and c) the coulombic efficiency of Si, Si–CuO and Si–CuO–NiO samples.

show a similar reaction mechanism to cr-Si but with an effective impediment on the generation of cr-$Li_{3.75}Si$.

Next, the cycle stabilities of the Si, Si–CuO, and Si–CuO–NiO samples are evaluated by presenting the 100-cycle data in Figures 6(a–c), with the quantitative data listed in Table 1. The highest initial delithiation capacity is observed for the pristine Si, which decreases with the introduction of more metal oxides, following a monotonic trend. The formation of the metal silicides and Si oxides[10,23,41] is responsible for the capacity decrease. However, the cycling stability of pristine Si is the poorest, with capacity retention of only 20.7% after 100 cycles (Figure 6b). A 3.7% (based on the atom ratio) addition of CuO into Si bulk can improve the cycling performance significantly, giving 74.1% capacity retention after 100 cycles, consistent with the previous reports.[27,28] As the CuO relative content further rises to 9.7%, the cycle performance of $Si_{90.3}(CuO)_{9.7}$ unexpectedly becomes worse, showing capacity retention of 59.6%. Such abnormal capacity degradation in Si–CuO samples may be related to the formation of Cu_2LiSi due to the lithiation of Cu_3Si, which could lead to the separation of Cu from Cu_3Si.[41] The deeper explanation requires further investigation. Regardless of the mechanism, these results imply that the improvement of CuO to the Si anodes will be restricted by its relative amount, and solely increasing the CuO ratio could not obtain an ideal cycle performance. Thus, the core strategy of this study is to replace a part of excessive CuO with NiO, where the advantages of CuO to the electrochemical performance are expected to be retained, and meanwhile, NiO is predicted to consume more active Si but not cause the deterioration of the cycle stability.[31] As we expected, the capacity retention after 100 cycles of Si–CuO–NiO samples continuously increases with more introduction of NiO, from 80.1% in $Si_{92.1}(CuO)_{3.6}(NiO)_{4.3}$ to 86.9% in $Si_{87.5}(CuO)_{3.4}(NiO)_{9.1}$. Moreover, the average coulombic efficiencies (ACE) in the Si–CuO–NiO samples are also noticeably improved (seen in Figure 6(c)), with the highest one

Table 1. The reversible capacity of 1st and 100th cycles, 100th-cycle capacity retention, and ACE of Si, Si–CuO, and Si–CuO–NiO samples.

Sample	1st reversible capacity [mAh g^{-1}]	100th reversible capacity [mAh g^{-1}]	100th Capacity retention [%], based on 2nd cycle	ACE [%], based on 2nd cycle
Si	2792	453	20.7	98.47
$Si_{96.3}(CuO)_{3.7}$	2771	1781	74.1	98.89
$Si_{90.3}(CuO)_{9.7}$	2052	1092	59.6	98.94
$Si_{92.1}(CuO)_{3.6}(NiO)_{4.3}$	2095	1471	80.1	99.06
$Si_{89.9}(CuO)_{3.5}(NiO)_{6.6}$	1821	1366	84.5	99.23
$Si_{87.5}(CuO)_{3.4}(NiO)_{9.1}$	1568	1208	86.9	99.40

Research Article
doi.org/10.1002/batt.202200495
Chemistry Europe
European Chemical Societies Publishing

observed in $Si_{87.5}(CuO)_{3.4}(NiO)_{9.1}$, giving an ACE of ~99.4% (seen in Table 1).

According to the method provided elsewhere[13] (the detailed calculation and result are presented in Figure S2), the Si–CuO–NiO samples are predicted to have less volume expansion during lithiation than the Si–CuO samples. Generally, the relatively mild volume change is beneficial to lessen crack formation, inhibit secondary SEI formation, and keep the integrity of the electrode for long-term cycling.[2,4–6] Then, we measure the thickness variation of the $Si_{96.3}(CuO)_{3.7}$, $Si_{89.9}(CuO)_{3.5}(NiO)_{6.6}$, and $Si_{87.5}(CuO)_{3.4}(NiO)_{9.1}$ electrodes before the cycling and after the second lithiation/delithiation (see in Figure 7). It can be seen that all the electrode thicknesses increase during lithiation but to a different degree, followed by volume contraction and recovery after full delithiation. To be specific, the swelling/contraction volume percentage in lithiation/delithiation for $Si_{96.3}(CuO)_{3.7}$, $Si_{89.9}(CuO)_{3.5}(NiO)_{6.6}$, and $Si_{87.5}(CuO)_{3.4}(NiO)_{9.1}$ is ~92.5%/38.3%, ~41.2%/16.7%, and ~38.9%/16.5%, respectively. The observation corresponds to the predicted trend by the theoretical calculation, and it indicates that with more introduction of NiO, the electrodes of Si–CuO–NiO could go through the less structural evolution during the cycles, which is assigned to be the main reason for the improved electrochemical performance.

Furthermore, the electrochemical impedance spectra (EIS) after the two cycles are measured (shown in Figures 7d, h, and l). The equivalent circuit model is inserted in Figure 7(d), where R_s represents the bulk resistance derived from the electrode, electrolyte, and separator; R_{sei} represents the SEI resistance with the corresponding capacitance referring to CPE1; R_{ct} represents the charge-transfer resistance with the corresponding capacitance referring to CPE2; W_o represents the Warburg impedance.[46] The fitting results imply that although the three samples have close R_{sei} after the two cycles, R_{ct} has an apparent reduction varying from 22.2 Ω in $Si_{96.3}(CuO)_{3.7}$ to 6.4 Ω in $Si_{87.5}(CuO)_{3.4}(NiO)_{9.1}$. The decreased impedance indicates that the ionic conductivity for the Si–CuO–NiO samples is improved,[47] which could be ascribed to the reduced volume change of Si-based particles rendering the more intact electrode, stable SEI, and better electrical contact. Therefore, combining the electrochemical tests, cross-section SEM images, and EIS analysis, we can conclude that adding NiO with a proper amount to the ball-milled Si–CuO samples could positively affect the electrochemical performance with further optimized capacity retention and ACE.

Lastly, it should be noted that the thermal stability of Si-based materials is vital since a carbon coating is considered the well-adopted post-processing step before the anode fabrication.[5,16,21] Generally, the sintering temperatures vary depending on different carbon precursors and coating methods, for example, changing from 400 °C to 900 °C.[9,45,48–53] In this study, $Si_{87.5}(CuO)_{3.4}(NiO)_{9.1}$ is selected to undergo an annealing step to test its thermal stability because of its best cycling stabilities. The annealing temperatures start from 600 °C, below which the evident growth of Si crystallites and metal silicides in $Si_{87.5}(CuO)_{3.4}(NiO)_{9.1}$ is not expected.[15,16]

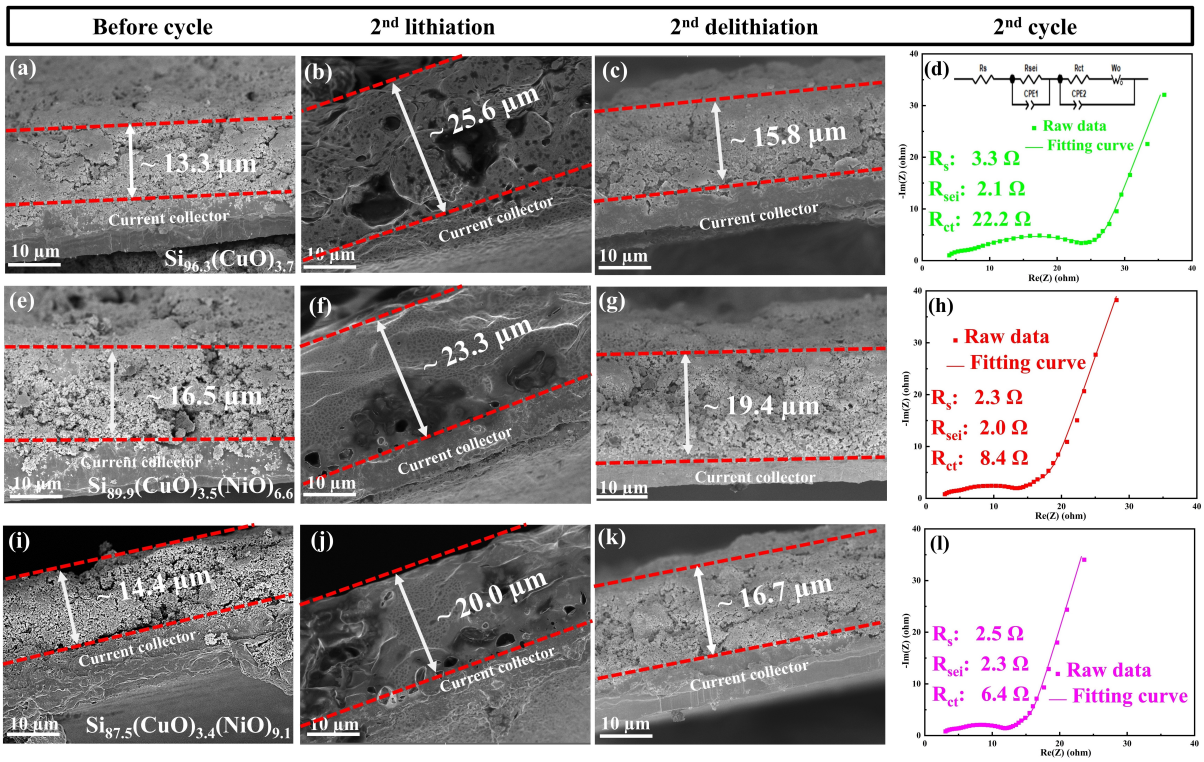

Figure 7. Cross-section SEM images of the $Si_{96.3}(CuO)_{3.7}$, $Si_{89.9}(CuO)_{3.5}(NiO)_{6.6}$, and $Si_{87.5}(CuO)_{3.4}(NiO)_{9.1}$ electrodes: a, e and i) before the cycle, b, f, and j) after the second lithiation, and c, g, and k) after the second delithiation. d, h, and l) Electrochemical impedance spectra (EIS) of $Si_{96.3}(CuO)_{3.7}$, $Si_{89.9}(CuO)_{3.5}(NiO)_{6.6}$, and $Si_{87.5}(CuO)_{3.4}(NiO)_{9.1}$ after the two cycles with the equivalent circuit model inserted in (d).

Research Article
doi.org/10.1002/batt.202200495
Chemistry Europe
European Chemical Societies Publishing

The x-ray diffractograms of annealed $Si_{87.5}(CuO)_{3.4}(NiO)_{9.1}$ are shown in Figure S3(a). It can be seen that all diffraction peaks become sharper and more recognizable, indicating higher crystallinity and bigger grain size of Si and metal silicides as compared to the ball-milled precursor. The grain size of Cu_3Si grows from ~37 nm in 600 °C to ~45 nm in 900 °C (seen in Figure S3b). Besides, the diffraction peaks assigned to Si oxides are absent in Figure S3(a), implying that an amorphous structure is properly maintained, which is considered beneficial for cycle stability.[21] TEM and STEM are conducted to characterize the change of microstructure and element distribution in the annealed $Si_{87.5}(CuO)_{3.4}(NiO)_{9.1}$. Figure S4 shows the BF and HRTEM images in the chosen regions. The microstructure of $Si_{87.5}(CuO)_{3.4}(NiO)_{9.1}$-600 still consists of dispersed nano-crystallites and amorphous regions. However, it has a noticeable transformation for $Si_{87.5}(CuO)_{3.4}(NiO)_{9.1}$-800 and $Si_{87.5}(CuO)_{3.4}(NiO)_{9.1}$-900, where the distribution of metal silicides starts to agglomerate and the rich-Cu_3Si or rich-$NiSi_2$ regions appear. This phenomenon is further confirmed by STEM results (Figure 8). Overall, the high-temperature annealing ≥ 800 °C could considerably change the uniform distribution of Cu and Ni in the $Si_{87.5}(CuO)_{3.4}(NiO)_{9.1}$ precursor.

The d*Q*/d*V* curves of sintered $Si_{87.5}(CuO)_{3.4}(NiO)_{9.1}$ and corresponding voltage-capacity curves are shown in Figure S5. There is no apparent difference in the curves between $Si_{87.5}(CuO)_{3.4}(NiO)_{9.1}$ and $Si_{87.5}(CuO)_{3.4}(NiO)_{9.1}$-600. However, the electrochemical behavior of the $Si_{87.5}(CuO)_{3.4}(NiO)_{9.1}$-800 and $Si_{87.5}(CuO)_{3.4}(NiO)_{9.1}$-900 becomes closer to the one of pristine Si, e.g., with the reappearance of the typical cr-$Li_{3.75}Si$ delithiation peak in the first d*Q*/d*V* curves. It may be because the formation of rich-Cu_3Si or rich-$NiSi_2$ regions decreases the contact areas between Si grains and metal silicides, causing inadequate suppression to the cr-$Li_{3.75}Si$ generation during the lithiation. Then, we calculate the capacity percentage derived from cr-$Li_{3.75}Si$ delithiation during the first cycle for Si, $Si_{87.5}(CuO)_{3.4}(NiO)_{9.1}$, $Si_{87.5}(CuO)_{3.4}(NiO)_{9.1}$-600, $Si_{87.5}(CuO)_{3.4}(NiO)_{9.1}$-800 and $Si_{87.5}(CuO)_{3.4}(NiO)_{9.1}$-900 via the method provided by the literature[42] (seen in Figure S6 and the corresponding

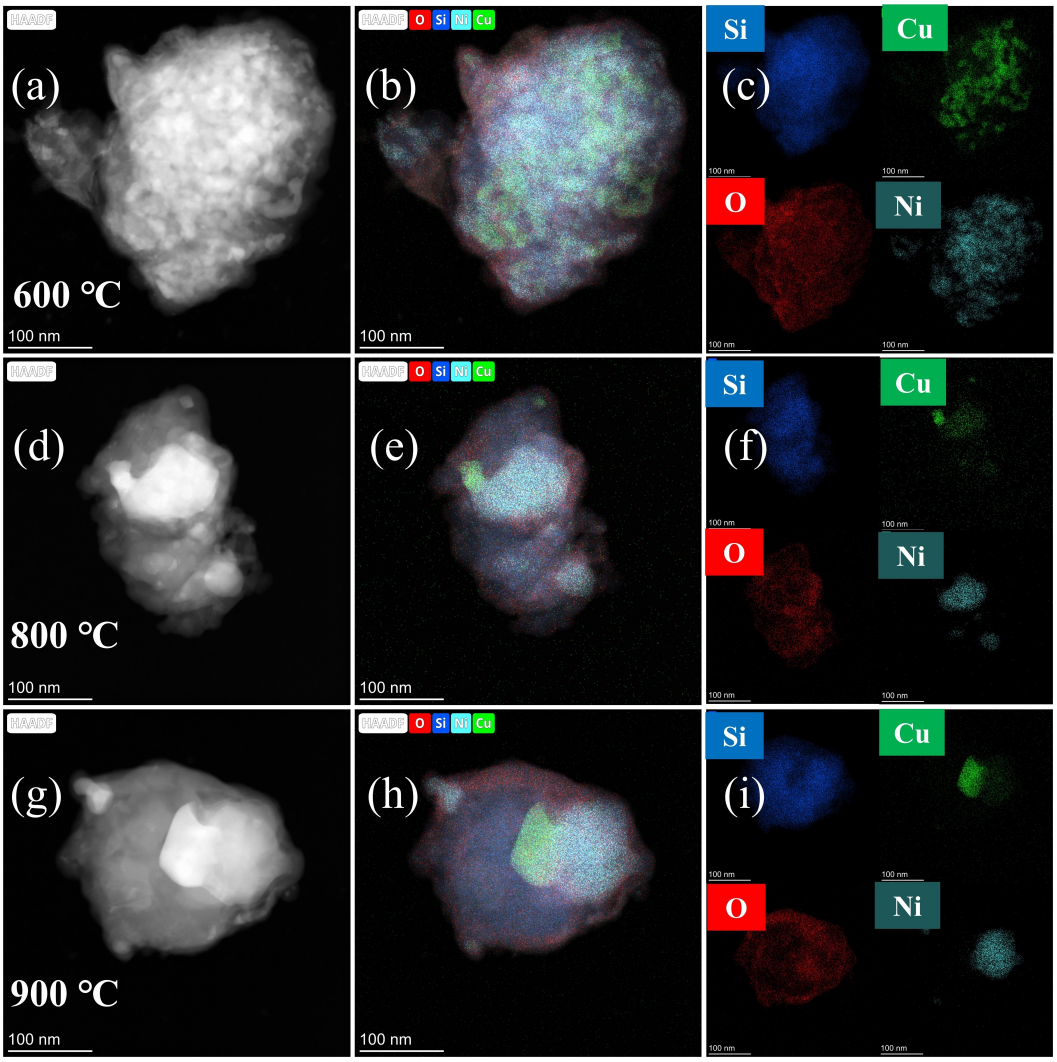

Figure 8. a, d and g) STEM images, b, e and h) element substitution overlaps, and c, f and i) element maps of $Si_{87.5}(CuO)_{3.4}(NiO)_{9.1}$-600, $Si_{87.5}(CuO)_{3.4}(NiO)_{9.1}$-800 and $Si_{87.5}(CuO)_{3.4}(NiO)_{9.1}$-900.

Research Article
doi.org/10.1002/batt.202200495
Chemistry Europe
European Chemical Societies Publishing

explanation). The percentage for $Si_{87.5}(CuO)_{3.4}(NiO)_{9.1}$ and $Si_{87.5}(CuO)_{3.4}(NiO)_{9.1}$-600 is at a comparable level with ~3%, whereas it has a significant increase for $Si_{87.5}(CuO)_{3.4}(NiO)_{9.1}$-800 and $Si_{87.5}(CuO)_{3.4}(NiO)_{9.1}$-900 with ~35% but still less than pristine Si with the value over 60%.

The 100-cycle performance of sintered $Si_{87.5}(CuO)_{3.4}(NiO)_{9.1}$ is provided in Figures 9(a, b), and $Si_{87.5}(CuO)_{3.4}(NiO)_{9.1}$-600 performs the highest capacity retention with ~91.2% even more than the one (~86.9%) in the $Si_{87.5}(CuO)_{3.4}(NiO)_{9.1}$. It may be due to the more sufficient reaction between Si and metal oxides via the sintering treatment. The value for $Si_{87.5}(CuO)_{3.4}(NiO)_{9.1}$-800 and $Si_{87.5}(CuO)_{3.4}(NiO)_{9.1}$-900 have different degrees of decline. Significantly, the cycle performance for $Si_{87.5}(CuO)_{3.4}(NiO)_{9.1}$-900 becomes much worse with only ~67.2% capacity retention. We ascribe it to the following reasons: 1) the re-generation of cr-$Li_{3.75}Si$ in the initial stage may accelerate the fragmentation of active materials and the crack formation on the electrode leading to the capacity loss;[40] 2) the metal silicide clusters will reduce the limitation to the growth of the Si grains, which is not conducive to the cycle stability;[13,14] 3) such clusters may impose uneven compressive stress (in lithiation) and tensile stress (in delithiation) on Si bulk causing severer structure breakduring cycling.[5,6] Therefore, we expect that a post-carbon-coating treatment conducted at 600 °C may obtain an optimized cycle performance for the ball-milled $Si_{87.5}(CuO)_{3.4}(NiO)_{9.1}$ precursor.

Then, polydopamine (PDA) is used as the carbon source to coat $Si_{87.5}(CuO)_{3.4}(NiO)_{9.1}$ at 600 °C, and the synthesized sample refers to $Si_{87.5}(CuO)_{3.4}(NiO)_{9.1}$@c-PDA. The TGA test in the air determines the amount of carbonized PDA (c-PDA) on the surface, and the result is shown in Figure S7 with a three-stage mass-changing process in the curve. Before 200 °C, a slight mass drop may be due to the water absorption loss. The carbonized temperature range is mainly from 200 °C to 500 °C with ~20% of the mass loss. Next, the mass increases at higher temperatures because the c-PDA is thoroughly consumed, and the pure Si is exposed to the air again and oxidized. The comparison of cycle performance and coulombic efficiency for $Si_{87.5}(CuO)_{3.4}(NiO)_{9.1}$ and $Si_{87.5}(CuO)_{3.4}(NiO)_{9.1}$@c-PDA is shown in Figures 9(c) and (d). After coating PDA, the 50-cycle capacity retention and the coulombic efficiency are further enhanced up to 95.8% and ~99.5%, respectively. In conclusion, when sintered at a suitable temperature, the ball-milled Si–CuO–NiO precursor could exert the maximized positive effect of a coated carbon layer on the electrochemical performance.

Conclusion

NiO has been adopted in this study to modify Si–CuO alloy anodes in LIBs via the HEBM method. The XRD, XPS, and TEM results reveal that the obtained Si–CuO–NiO samples mainly consist of nanocrystalline Si, doped metal silicides, and

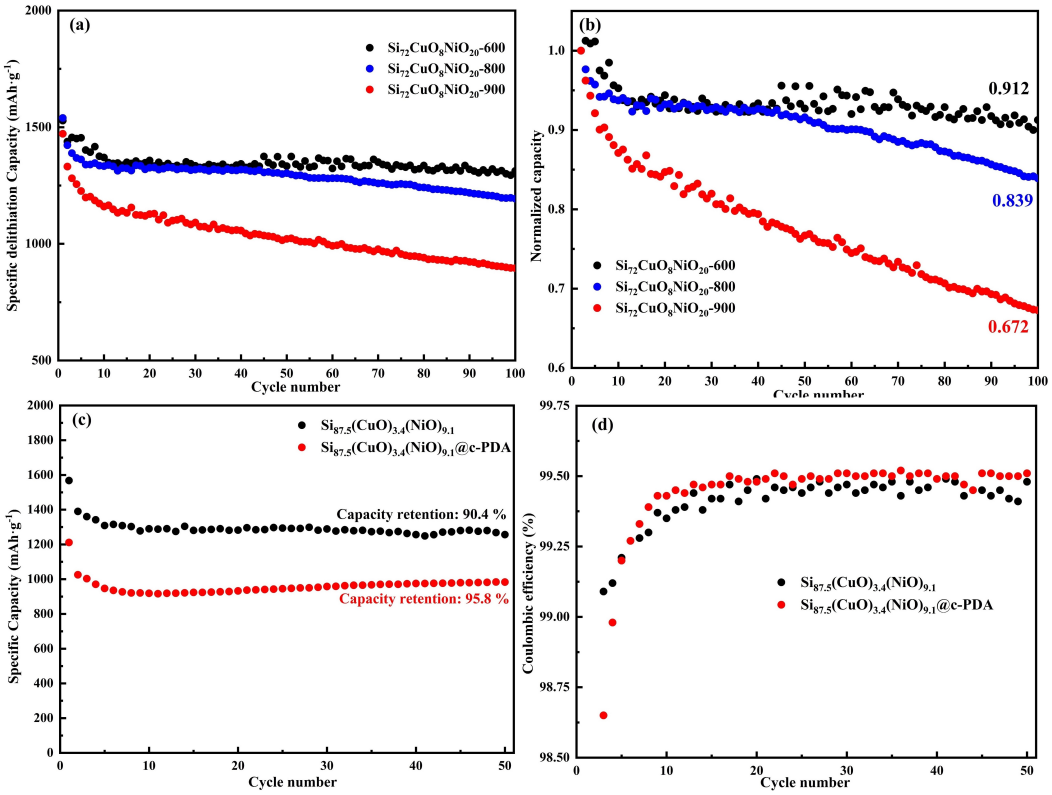

Figure 9. a) Specific delithiation capacity vs. cycle number and b) normalized delithiation capacity vs. cycle number (based on the second cycle) of $Si_{87.5}(CuO)_{3.4}(NiO)_{9.1}$-600, $Si_{87.5}(CuO)_{3.4}(NiO)_{9.1}$-800 and $Si_{87.5}(CuO)_{3.4}(NiO)_{9.1}$-900. c) Specific delithiation capacity vs. cycle number and d) the coulombic efficiency (from the 3rd cycle) of $Si_{87.5}(CuO)_{3.4}(NiO)_{9.1}$ and $Si_{87.5}(CuO)_{3.4}(NiO)_{9.1}$@c-PDA.

amorphous Si oxides. The electrochemical analysis indicates that adding NiO would not cause evident differences in the reaction mechanisms with the Si–CuO samples. Although the formation of cr-$Li_{3.75}Si$ can be effectively suppressed for all ball-milled samples, a higher CuO addition (9.7%) is observed to deteriorate the cycle performance severely. Using NiO to replace a part of CuO is suggested to be useful in mitigating this issue, giving an enhanced electrochemical performance due to less volume change and reduced impedance. In addition, the thermal stability test, and the post-carbon-coating treatment show that the ball-milled Si–CuO–NiO precursor should be sintered at no more than 800 °C. The optimization of the CuO/NiO ratio and the carbon coating is expected in further investigation.

Experimental

Synthesis of Si–CuO/Si–CuO–NiO samples

The samples are synthesized by the high-energy ball-milling machine (Model HCX-YY-TC-2 L, Kunming Haichuangxing Technology Co., Ltd., Yunnan, China). The mass ratio of ZrO_2 balls ($\varnothing$ = 3 mm; 1.8 kg) to the added Si-based powders (90 g) is 20:1, and the rotation speed is set at 1200 rpm. To start with, we introduce a protective gas (Ar) into the milling chamber. The total milling time is 4 h, and ~0.5 g powder samples are taken out per hour to undergo the X-ray diffraction (XRD) test. The raw Si powder in our study has a medium particle size of ~4 μm (Zhejiang Lichen New Materials Technology Co., Ltd, China), and the CuO (99.5%, 100–200 nm) and NiO powder (99.0%, −325 mesh) is purchased from Macklin and Aladdin in China, respectively. The initial mass and atom ratios of Si, CuO, and NiO for each sample are shown in Table S1. The latter is adopted to represent samples, referring to Si, $Si_{96.3}(CuO)_{3.7}$, $Si_{90.3}(CuO)_{9.7}$, $Si_{92.1}(CuO)_{3.6}(NiO)_{4.3}$, $Si_{89.9}(CuO)_{3.5}(NiO)_{6.6}$, and $Si_{87.5}(CuO)_{3.4}(NiO)_{9.1}$. The preparation of $Si_{96.3}(CuO)_{3.7}$ and $Si_{90.3}(CuO)_{9.7}$ is for comparison to represent 0% NiO samples. Lastly, $Si_{87.5}(CuO)_{3.4}(NiO)_{9.1}$ is chosen for the assessment of high-temperature tolerance sintered at 600, 800, and 900 °C for 3 h in the Ar atmosphere, referring to $Si_{87.5}(CuO)_{3.4}(NiO)_{9.1}$-600, $Si_{87.5}(CuO)_{3.4}(NiO)_{9.1}$-800 and $Si_{87.5}(CuO)_{3.4}(NiO)_{9.1}$-900, respectively.

Lastly, polydopamine (PDA) is used as the carbon source to coat $Si_{87.5}(CuO)_{3.4}(NiO)_{9.1}$. In a typical procedure, we add 0.4851 g of Tris base (99.99%, Aladdin) and ~0.1 mL of the hydrochloric acid (the mass percentage = 37%) to 400 mL of the deionized water adjusting the pH value to ~8.5, respectively. Then, 0.2 g of $Si_{87.5}(CuO)_{3.4}(NiO)_{9.1}$ and 0.2 g of dopamine hydrochloride (98%, Aladdin) are added into the solution together with stirring for 10 h at room temperature. Next, the suspension is filtered and washed with the deionized water at least five times and then dried at 100 °C in a vacuum overnight, followed by the annealing treatment at 600 °C for 3 h in the Ar atmosphere. The final product refers to $Si_{87.5}(CuO)_{3.4}(NiO)_{9.1}$@c-PDA.

Material characterization

The phase structures of all the samples are determined by a Panalytical desktop Aeris X-ray diffraction (XRD, Cu K_α) equipment from 10° to 80° with a scanning rate of 5°/min. Field emission scanning electron microscopies are used to observe the particle morphologies and the thickness change of electrodes (FESEM, ZEISS Sigma 300, Germany, and Tescan MAIA3, respectively). Transmission electron microscopy (TEM), high-resolution lattices of the chosen materials, selected area electron diffraction (SAED), scanning TEM (STEM) images, and element mappings are conducted by TEM (Talos F200x G2) for confirming the microstructure and the element distribution of the samples. X-ray photoelectron spectroscopy (XPS) is performed on Thermo ESCALAB 250XI to analyze the chemical state of the elements in the samples. The particle size of the samples is determined through a particle size analyzer (Malvern Mastersizer 2000, UK), and the true density of ball-milled samples is measured by a fully automatic density analyzer (AccuPyc II 1340, USA). The thermogravimetric analysis (TGA, TGA5500, USA) is employed to determine the content of the coated carbon layer at 10 °C/min from room temperature to 800 °C in air.

Cell preparation and testing

The electrochemical performance is evaluated with CR2025-type coin cells. The electrode slurries are prepared by mixing the active material, Super P and CMC–Na (sodium carboxymethyl cellulose, viscosity: 1000–1400 mPas, Aladdin)/PAA (polyacrylic acid, M_v ~3,000,000, Aladdin) in the mass ratio of 70:15:7.5:7.5 in deionized water. The working electrodes are fabricated by uniformly coating the slurries onto the Cu foil current collector with an initial area capacity level of 2.1–2.6 $mAh{\cdot}cm^{-2}$ (or the mass loading in the range from 0.7–1.3 $mg\,cm^{-2}$). Then electrodes are dried in a vacuum at 80 °C for 12 h, followed by 150 °C for one hour. The prepared electrode sheet is cut into small disk electrodes with a diameter of 12 mm. With the Li foil as a counter electrode, the coin cells are assembled in an argon-filled glovebox ($H_2O \leq$ 0.5 ppm, $O_2 \leq 0.5$ ppm) (MBRAUN, Germany). The electrode separator is a Celgard 2400 membrane, and the electrolyte was a 1 M $LiPF_6$ solution in a mixture of ethylene carbonate (EC) and dimethyl carbonate (DMC) at a volume ratio of 1:1 with 10% (volume) FEC (fluoroethylene carbonate) as the additive. The C-rate is determined by applying the current density of 100 $mA\,g^{-1}$ during the first cycle for all cells, and the obtained lithiation capacity is adopted as 1 C. Then, all cells are cycled under the current density of 0.2 C in the voltage range of 0.01–1 V versus Li/Li^+ since the second cycle. Electrochemical impedance spectroscopy (EIS) is tested at a voltage amplitude of 10 mV with a frequency range from 1 MHz to 0.01 Hz (Biologic, VMP300, France).

Acknowledgements

The work was supported financially by the Hong Kong Polytechnic University and the University of Glasgow. Special thanks to Dr. Zhou Ruitao for the helpful discussion and Shiyanjia Lab (www.Shiyanjia.com) for technical support on the testing of TEM/HRTEM.

Conflict of Interest

There are no conflicts to declare.

Data Availability Statement

The data that support the findings of this study are available from the corresponding author upon reasonable request.

Keywords: CuO and NiO doping · high-energy ball-milling method · lithium-ion batteries · silicon-based alloy anodes · thermal stability

[1] P. Li, H. Kim, S. T. Myung, Y. K. Sun, *Energy Storage Mater.* **2021**, *35*, 550–576.
[2] M. N. Obrovac, *Curr. Opin. Electrochem.* **2018**, *9*, 8–17.
[3] M. N. Obrovac, V. L. Chevrier, *Chem. Rev.* **2014**, *114*, 11444–11502.
[4] Z. J. Du, R. A. Dunlap, M. N. Obrovac, *J. Electrochem. Soc.* **2014**, *161*, A1698-A1705.
[5] S. M. Cao, M. H. Tahmasebi, J. C. Bennett, M. N. Obrovac, *Electrochim. Acta* **2021**, *396*, 139259.
[6] S. M. Cao, J. C. Bennett, Y. K. Wang, S. Gracious, M. Zhu, M. N. Obrovac, *J. Power Sources* **2019**, *438*, 227003.
[7] M. Kim, Z. Yang, I. Bloom, *J. Electrochem. Soc.* **2021**, *168*, 010523.
[8] M. Ruttert, V. Siozios, M. Winter, T. Placke, *ACS Appl. Energ. Mater.* **2020**, *3*, 743–758.
[9] S. S. Lee, K. H. Nam, H. Jung, C. M. Park, *Chem. Eng. J.* **2020**, *381*, 122619.
[10] Z. J. Du, T. D. Hatchard, P. Bissonnette, R. A. Dunlap, M. N. Obrovac, *J. Electrochem. Soc.* **2016**, *163*, A2456-A2460.
[11] Z. J. Du, T. D. Hatchard, R. A. Dunlap, M. N. Obrovac, *J. Electrochem. Soc.* **2015**, *162*, A1858-A1863.
[12] M. N. Obrovac, L. Christensen, D. B. Le, J. R. Dahn, *J. Electrochem. Soc.* **2007**, *154*, A849-A855.
[13] M. T. McDowell, S. W. Lee, J. T. Harris, B. A. Korgel, C. Wang, W. D. Nix, Y. Cui, *Nano Lett.* **2013**, *13*, 758–764.
[14] X. H. Liu, L. Zhong, S. Huang, S. X. Mao, T. Zhu, J. Y. Huang, *ACS Nano* **2012**, *6*, 1522–1531.
[15] S. M. Cao, S. Gracious, J. C. Bennett, M. N. Obrovac, *J. Electrochem. Soc.* **2020**, *167*, 130531.
[16] Y. J. Liu, C. Bennett, M. N. Obrovac, *J. Electrochem. Soc.* **2019**, *166*, A2791-A2796.
[17] Y. D. Cao, J. C. Bennett, R. A. Dunlap, M. N. Obrovac, *J. Electrochem. Soc.* **2018**, *165*, A1734-A1740.
[18] Y. K. Wang, S. M. Cao, M. Kalinina, L. T. Zheng, L. J. Li, M. Zhu, M. N. Obrovac, *J. Electrochem. Soc.* **2017**, *164*, A3006-A3010.
[19] Z. J. Du, S. N. Ellis, R. A. Dunlap, M. N. Obrovac, *J. Electrochem. Soc.* **2016**, *163*, A13-A18.
[20] Y. Zhang, C. Y. Zhu, Z. H. Ma, *J. Alloys Compd.* **2021**, *851*, 156854.
[21] Y. J. Liu, M. Charlton, J. Wang, J. C. Bennett, M. N. Obrovac, *J. Electrochem. Soc.* **2021**, *168*, 110521.
[22] X. Y. Zhao, R. J. Sanderson, M. A. Al-Maghrabi, R. A. Dunlap, M. N. Obrovac, *J. Electrochem. Soc.* **2017**, *164*, A1165-A1172.
[23] Z. Liu, Q. Yu, Y. Zhao, R. He, M. Xu, S. Feng, S. Li, L. Zhou, L. Mai, *Chem. Soc. Rev.* **2019**, *48*, 285–309.
[24] Y. D. Cao, J. C. Bennett, R. A. Dunlap, M. N. Obrovac, *Chem. Mater.* **2018**, *30*, 7418–7422.
[25] A. Hohl, T. Wieder, P. A. van Aken, T. E. Weirich, G. Denninger, M. Vidal, S. Oswald, C. Deneke, J. Mayer, H. Fuess, *J. Non-Cryst. Solids* **2003**, *320*, 255–280.
[26] L. Shi, Y. Li, Y. Xing, R. Q. Lin, G. G. Cheng, J. N. Ding, K. H. Lam, *Electrochim. Acta* **2021**, *390*, 138841.
[27] S. C. Hou, T. Y. Chen, Y. H. Wu, H. Y. Chen, X. D. Lin, Y. Q. Chen, J. L. Huang, C. C. Chang, *Sci. Rep.* **2018**, *8*, 12695.
[28] Y. H. Wu, O. L. Huang, S. C. E. Hou, M. C. Tsai, C. C. Chang, *Electrochim. Acta* **2021**, *387*, 138495.
[29] H. Liu, Y. Chen, Z. Wang, C. Zhang, X. Zhang, W. Zhou, J. Liu, W. Wang, P. Yu, *J. Alloys Compd.* **2022**, *905*, 164207.
[30] S. O. Kim, A. Manthiram, *J. Mater. Chem. A* **2015**, *3*, 2399–2406.
[31] Z. J. Du, S. N. Ellis, R. A. Dunlap, M. N. Obrovac, *J. Electrochem. Soc.* **2016**, *162*, A13-A18.
[32] E. G. Barbagiovanni, L. V. Goncharova, P. J. Simpson, *Phys. Rev. B* **2011**, *83*, 035112.
[33] W. F. Banholzer, M. C. Burrell, *Surf. Sci.* **1986**, *176*, 125–133.
[34] Y. Cao, L. Nyborg, U. Jelvestam, *Surf. Interface Anal.* **2009**, *41*, 471–483.
[35] S. Valeri, U. D. Pennino, P. Sassaroli, *Surf. Sci.* **1983**, *134*, L537-L542.
[36] N. Weidler, J. Schuch, F. Knaus, P. Stenner, S. Hoch, A. Maljusch, R. Schäfer, B. Kaiser, W. Jaegermann, *J. Phys. Chem. C* **2017**, *121*, 6455–6463.
[37] J. Y. Woo, A. Y. Kim, M. K. Kim, S. H. Lee, Y. K. Sun, G. C. Liu, J. K. Lee, *J. Alloys Compd.* **2017**, *701*, 8.
[38] Jing Li, J. R. Dahn, *J. Electrochem. Soc.* **2007**, *154*, A156-A161.
[39] M. N. Obrovac, L. J. Krause, *J. Electrochem. Soc.* **2007**, *154*, A103-A108.
[40] M. N. Obrovac, L. Christensen, *Electrochem. Solid-State Lett.* **2004**, *7*, A93-A96.
[41] Z. J. Du, H. Liu, S. N. Ellis, R. A. Dunlap, M. Zhu, M. N. Obrovac, *J. Electrochem. Soc.* **2016**, *163*, A1275-A1279.
[42] Y. D. Cao, B. Scott, R. A. Dunlap, J. Wang, M. N. Obrovac, *J. Electrochem. Soc.* **2019**, *166*, A21-A26.
[43] X. G. Liu, N. N. Bi, C. Feng, S. W. Or, Y. P. Sun, C. G. Jin, W. H. Li, F. Xiao, *J. Alloys Compd.* **2014**, *587*, 1–5.
[44] Y. Liu, W. L. Peng, J. H. Zhang, S. B. Li, R. Z. Hu, B. Yuan, G. J. Chen, *J. Alloys Compd.* **2022**, *918*, 165693.
[45] B. Kim, J. Ahn, Y. Oh, J. Tan, D. Lee, J.-K. Lee, J. Moon, *J. Mater. Chem. A* **2018**, *6*, 3028–3037.
[46] R. Maddipatla, C. Loka, W. Choi, K. S. Lee, *Appl. Sci.* **2018**, *8*, 2140.
[47] R. Maddipatla, C. Loka, K. S. Lee, *ACS Appl. Mater. Interfaces* **2020**, *12*, 54608–54618.
[48] R. Miao, J. Zhu, S. Kang, J. Yang, J. Wang, J. Fu, M. Li, C. Shi, *Electrochim. Acta* **2021**, *384*, 138413.
[49] M. Ashuri, Q. He, L. L. Shaw, *J. Electroanal. Chem.* **2020**, *876*, 114738.
[50] J. H. Kim, H. Kim, H. J. Sohn, *Electrochem. Commun.* **2005**, *7*, 557–561.
[51] Q. H. Lian, Y. Q. Lu, W. Q. Ding, X. D. He, Z. M. Zou, C. H. Jiang, *Appl. Surf. Sci.* **2022**, *592*, 153322.
[52] S. Suh, H. Yoon, H. Park, J. Kim, H. J. Kim, *Appl. Surf. Sci.* **2021**, *567*, 150868.
[53] J. K. Ma, Y. X. Zheng, Y. P. Gan, J. Zhang, Y. Xia, X. P. He, W. K. Zhang, H. Huang, *J. Electron. Mater.* **2022**, *51*, 4780–4789.

Manuscript received: November 11, 2022
Revised manuscript received: January 20, 2023
Accepted manuscript online: January 23, 2023
Version of record online: March 27, 2023